

Analyzing Radial Velocity Data from the Resonant Planetary System HD 45364

IAN CHOW

ADVISORS: SAM HADDEN AND HANNO REIN

1. INTRODUCTION

During the past decade, a number of multiple-planet exoplanetary systems have been discovered. Radial velocity (RV) fitting has revealed many of these systems to contain planets in mean-motion resonance, in which their periods are related by a small integer ratio. These resonances usually form as a result of convergent orbital migration of planets (Goldreich 1965), a process which can occur due to planet interactions with a protoplanetary disk (Goldreich & Tremaine 1980). As such disk interactions are relatively common in planet formation, resonant systems present as the archetypal results of convergent orbital migration. Thus, systems hosting resonant planets present attractive choices for studying orbital migration and its role in planetary formation.

In this paper, we analyse the planetary system HD 45364, consisting of a roughly solar-mass star ($\sim 0.88M_{\odot}$) with two large (Jupiter-mass) planets orbiting in a 3:2 mean motion resonance. The system was first discovered by Correia et al. (2009) and was most recently studied by Hadden & Payne (2020). New RV data on the system has since become available from the HARPS-RVBank archive (Trifonov et al. 2020). We first generate a radial velocity curve from planet parameters using n -body integration and fit it to the new HARPS data. We also perform Markov chain Monte Carlo (MCMC) sampling to derive the posterior probability distributions for all parameters, of which the most useful are the 2-D marginal posteriors for the planets' masses and eccentricities. Our best-fit solution for the RV curve and posterior distributions are then used to derive tighter constraints on the masses of HD 45364's planets. Finally, we develop a model for the planets' capture into orbital resonance and test it by comparing its results to the observed parameters.

1.1. Strongly Interacting Systems

Since the planets orbiting HD 45364 are large and close together, the system is strongly gravitationally interacting. This has significant consequences for our analysis, the most important of which is the need for n -body simulation. RV data is usually fit by approximating each planet's orbit as Keplerian and then summing their individual RV signals, an approach which is com-

putationally inexpensive due to analytic solutions for Keplerian orbits. However, HD 45364 must instead be modelled as the more general n -body problem, which is analytically intractable. We therefore use numerical n -body integration methods to simulate HD 45364 instead. All n -body simulations in this paper are conducted using the `rebound` (Rein & Liu 2012) package in Python.

In addition, the strongly interacting nature of HD 45364 allows us to derive overall tighter constraints on planet parameters. Usually, only the radial component of a star's velocity can be seen in RV data. It is therefore difficult to determine whether a given RV signal is from a more-massive planet on a highly-inclined orbit or a less-massive planet on a less-inclined orbit. Due to this degeneracy in planet inclination, it is generally possible to derive only lower bounds on planet masses from RV data. Indeed, previous studies of HD 45364 (e.g. Hadden & Payne (2020)) have only reported minimum planet masses ($m \sin i$). However, the high minimum masses and close orbits of HD 45364's planets means the system becomes chaotic and dynamically unstable if the planets are too large. Since unstable orbital configurations will result in poorly-fitting RV signals, this can be exploited to determine upper bounds for the planets' masses, as well as overall tighter constraints on planet parameters compared to previous results.

2. RESONANCE DYNAMICS

The process of resonance capture begins when migration forces drive both planets' orbits inwards. As the migration rate for each planet depends in general on its mass, differing rates between planets can result in convergent migration into a resonant configuration. If the rate of migration and the planets' eccentricities are both sufficiently small, tidal interactions between the planets keep them in resonance (Goldreich 1965) while their eccentricities start to increase. As the eccentricities continue to grow, the planets eventually move too far enough away from each other for such interactions to maintain the resonance. However, if the planets are also subject to eccentricity damping forces, the planets will stay in resonance and their eccentricities will reach equilibrium values based on the relative strengths of the migration and eccentricity damping forces. Fig-

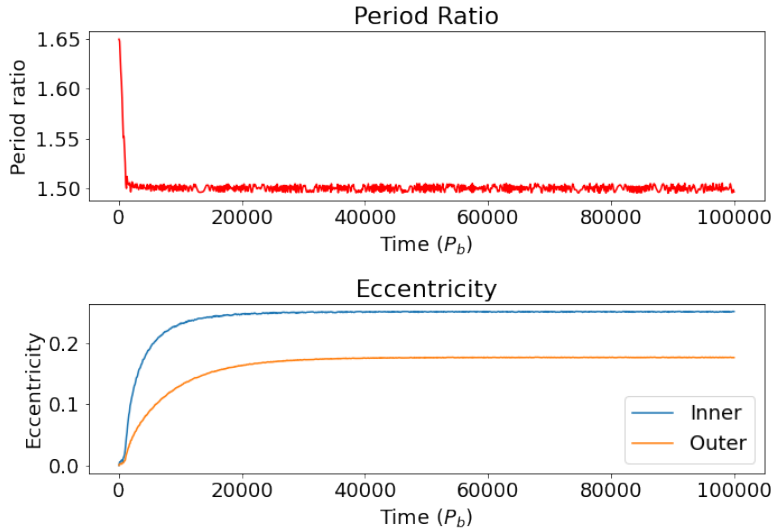


Figure 1. N -body simulation of the resonance capture process for HD 45364, taking place over 100000 orbits of the inner planet. The simulation is initialized using coplanar planets in circular orbits, a period ratio of $\frac{P_c}{P_b} = 1.1 \frac{3}{2}$ (slightly greater than the resonant period ratio of $\frac{3}{2}$), and with planet masses taken as the best-fit minimum masses from Fig. 2. The time axis is in units of P_b , the orbital period of the inner planet. The planets undergo convergent migration into a 3:2 resonance, and remain in resonance as their eccentricities continue to grow, eventually reaching equilibrium values.

ure 1 provides a demonstration of this process. Rein, Papaloizou, & Kley (2009) found that migration and eccentricity damping forces in HD 45364 could arise from interactions between planets and a protoplanetary accretion disk. Our primary goal is thus to analyze the final orbital configurations produced by the aforementioned resonance capture process to determine whether they compare favourably to observations.

3. RADIAL VELOCITY FITTING

We parameterize the system using 5 parameters for each planet: its semi-amplitude k (half the peak-to-peak amplitude of its RV signal), period P , eccentricity e , time of conjunction T , and argument of pericenter ω . A planet’s minimum mass can be computed from its semi-amplitude k as follows:

$$m_i \sin i = \left(\frac{2\pi G}{P_i} \right)^{-1/3} M^{2/3} k_i \sqrt{1 - e_i^2} \quad (1)$$

where M is the mass of the parent star. A full derivation of Equation 1 can be found in Perryman (2018). Our model also includes parameters for the star’s overall radial velocity offset γ and the sine of the orbital inclination $\sin i$, with the planets assumed to be coplanar. Using n -body simulation, we generate an RV curve

from the planet parameters, which we fit to data using least-squares optimization to find best-fit parameters

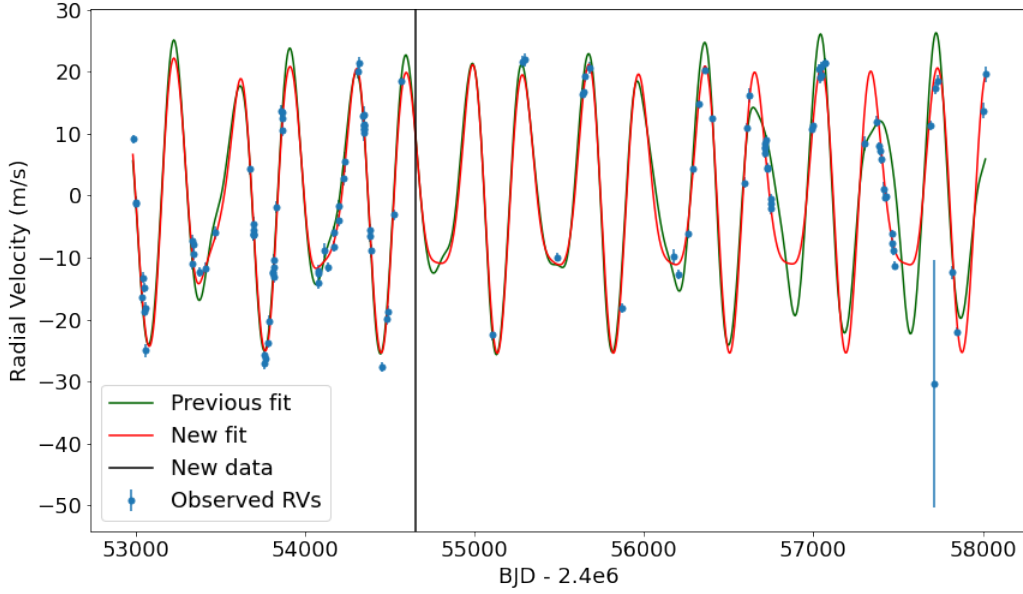
3.1. Bayesian Inference and MCMC Sampling

We also construct posterior distributions for each parameter to determine uncertainties. To do so, we use Bayesian inference on a prior model M for a set of data \mathbf{x} . The posterior distribution $P(\theta|\mathbf{x}, M)$ for a set of system parameters θ is then given by Bayes’ theorem:

$$P(\theta|\mathbf{x}, M) = \frac{P(\mathbf{x}|\theta, M) P(\theta|M)}{P(\mathbf{x}|M)} \quad (2)$$

where $P(\mathbf{x}|\theta, M)$ is the likelihood function, $P(\theta|M)$ is the prior, and $P(\mathbf{x}|M)$ is the marginal likelihood. Our goal is to determine the posterior distribution, which represents the distribution of the parameters θ after taking into account the observed data, a problem which is for high-dimensional models (such as ours) analytically intractable in general. As such, we use Markov chain Monte Carlo (MCMC) sampling to approximate the posterior distribution, which works by drawing samples from a given prior distribution with a number of chains. Each chain’s position is updated for the next sample based on the probability of the likelihood function, and the approximate posterior distribution is then constructed using all the samples.

In our MCMC sampling procedure, we adopt uniform priors across all parameters in the model, with some restrictions based on physical interpretation of parameters: the planet period P , minimum mass $m \sin i$, and time of conjunction T are all restricted to be positive, while the eccentricity e and sine of inclination $\sin i$ are restricted to the range $[0, 1]$. We use 50000 MCMC samples across 50 chains, initialized in a small radius around the best-fit parameters from Fig. 2, to construct marginal 1 and 2-D posterior distributions for all parameters in the model. All MCMC sampling in this paper is implemented using the `emcee` (Foreman-Mackey et al. 2013) software package in Python. The results of our radial velocity fit, as well as percentiles of the marginal 1-D posterior distribution of each parameter, can be found in Fig. 2. Our n -body model using the new HARPS data produces a better fit compared to previous results, preferred both by the least-squares χ^2 cost function as well as by the negative log-probability of our MCMC posterior distribution. We also obtain overall improved bounds from the posterior distribution of parameters such as eccentricities. Moreover, the system’s dynamical instability allows us to constrain the orbital inclination $\sin i$ (as noted in Section 1.1), allowing us to construct a 2-D marginal posterior distribution for the planet masses m_b and m_c by dividing the



Parameter	HARPS <i>N</i> -body fit			Previous <i>N</i> -body fit		
χ^2	278			2022		
$-\log(p(\mathbf{x} \theta, M))$	269			2012		
	5%	Best-fit	95%	5%	50%	95%
$m_b \sin i (M_J)$	0.19	0.20	0.21	0.16	0.18	0.20
P_b (days)	228.09	228.51	228.93	222.86	224.83	226.61
e_b	0.016	0.033	0.066	0.05	0.17	0.28
T_b (BJD - 2.4×10^6 days)	53934.70	53937.40	53940.18			
M_b				1.40	2.10	2.60
ω_b	-2.18	-1.89	-1.16	-3.10	2.64	3.10
$m_c \sin i (M_J)$	0.56	0.56	0.57	0.55	0.60	0.65
P_c (days)	343.12	343.38	343.63	342.47	343.96	345.55
e_c	0.0074	0.027	0.051	0.02	0.08	0.14
T_c (BJD - 2.4×10^6 days)	54017.11	54018.64	54020.17			
M_c				3.91	4.55	5.11
ω_c	0.86	0.94	1.16	-0.33	0.22	0.85
γ (m/s)	-0.67	-0.53	-0.39	-0.87	-0.0033	0.93
$\sin i$	0.86	1	1			

Figure 2. Parameters for our RV fit. Top: Comparison of our fit RV curve (in red) with the previous best fit, over a period of approximately 5000 days. Observed data points with errorbars are shown in blue. The points to the right of the black line are new data from the HARPS-RVBank archive. Time is given as the Barycentric Julian Date (BJD) - 2.4×10^6 days. Bottom: Comparison of our best-fit solutions for planet parameters (using the HARPS data) with previous results from [Hadden & Payne \(2020\)](#). A 90% credible interval using each parameter’s 1-D marginal posterior distribution is shown. Note that the negative log-probabilities for both fits are evaluated over *our* computed posterior distributions. In addition, we parameterize the orientation of the planets’ orbits using the time of conjunction T , while [Hadden & Payne \(2020\)](#) use the mean anomaly M instead. We also use the system’s dynamical instability to produce constraints on $\sin i$, the inclination of the planets’ orbits.

minimum masses $m \sin i$ of each MCMC sample by $\sin i$. This allows us to derive upper bounds on planet masses, which has not been done previously for this system. Fig. 3 shows our marginal posterior distribution, with the best-fit solution and quantiles marked. We then use the 5% and 95% quantiles of the mass posterior distribution to construct a 90% Bayesian credible interval on our prior, yielding upper and lower bounds of $0.20M_J \leq m_b \leq 0.23M_J$ and $0.56M_J \leq m_c \leq 0.66M_J$.

3.2. Orbital Migration and Eccentricity Damping

To determine whether HD 45364’s orbital configuration can be modelled using the resonance capture process described earlier, we simulate the system under migration and eccentricity damping forces (as shown in Fig. 1) and compare the equilibrium eccentricities to the observed values of the system. For our simulations, we adopt a simple model of exponential decay for the eccentricity e and semi-major axis ratio a . This is param-

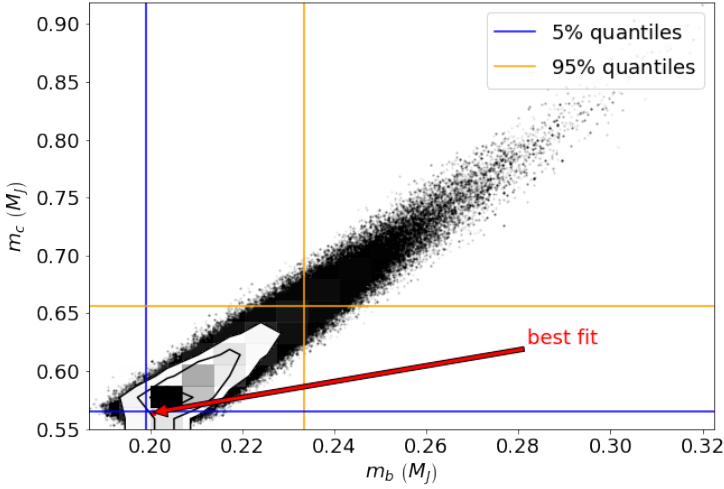


Figure 3. Marginal 2-D posterior distribution of planet masses obtained from MCMC sampling. Most samples lie near the bottom left (evinced by the contour lines and density colourmap) of a diagonal strip that rapidly tapers off with rising mass, due to dynamical instability that arises when the planets become large. We thus obtain quite restrictive upper bounds on the planet masses, which we take as the 95th percentile of the marginal distribution.

eterized as $e(t) = e_0 e^{-t/\tau_e}$ and $a(t) = a_0 e^{-t/\tau_a}$, where τ_e is the eccentricity damping timescale (shared by both planets) and τ_a is the convergent migration timescale, on which the ratio of the two planets’ semi-major axes decays. Since the migration rate for planets in general differs depending on their mass (see Appendix A), we use the individual migration timescales for each planet τ_{a_b}, τ_{a_c} in our simulations. These can be computed from the convergent migration timescale τ_a as follows:

$$\begin{bmatrix} 1/\tau_{a_b} \\ 1/\tau_{a_c} \end{bmatrix} = \begin{bmatrix} -1 & 1 \\ m_b & m_c \left(\frac{a_b}{a_c} \right)_r \end{bmatrix}^{-1} \begin{bmatrix} -1/\tau_a \\ 0 \end{bmatrix} \quad (3)$$

where m_b, m_c are the planet masses and $\left(\frac{a_b}{a_c} \right)_r$ is the resonant semi-major axis ratio. A complete derivation of equation 3 can be found in Appendix A. The dynamics of the system under migration and eccentricity damping forces, including the equilibrium eccentricities, are only affected by the ratio of the two timescales τ_a/τ_e which we denote K . We therefore initialize many simulations, each with a different value of K , and integrate until the planets reach their equilibrium eccentricities (like in Fig. 1). Plotting these equilibrium values in e_1 - e_2 phase space then creates an eccentricity “track,” where each point represents the equilibrium eccentricities for a certain K . We then compare this eccentricity track to our 2-D marginal eccentricity posterior to determine where they overlap, as shown in Fig. 4. Points on the the track overlapping the eccentricity distribution thus

correspond to values of K which produce equilibrium eccentricities consistent with the observed posterior; i.e. values of K for which the model’s results match the current configuration of the system. Our results from Fig. 4 therefore suggest that our migration-eccentricity damping model accurately predicts the current orbital eccentricities of the planets, for values of K between roughly $50 < K < 200$.

We conduct 300 n -body simulations in total, for K ranging from $K = 1$ to $K = 10^5$. As in Fig. 1, each simulation was initialized using the best-fit planet masses, with the planets in circular ($e = 0$) coplanar orbits and the ratio of the two planets’ semi-major axes just outside the resonant value. The simulations were performed using **rebound** in Python, while migration and eccentricity damping of orbits were implemented using the **reboundx** (Tamayo et al. 2020) package.

4. CONCLUSIONS

In this paper, we analyzed new RV data from the planetary system HD 45364 to develop a model for the formation of orbital resonance in the system, with our results summarized as follows:

We fit an RV curve from an n -body simulation to observed data, using least-squares optimization to solve for a best-fit set of parameters for the system, while MCMC sampling was used to approximate the posterior probability distributions for all parameters. Our results, summarized in Fig. 2, present an overall improvement over previous parameter estimates of the system. We also exploited the system’s dynamical instability in order to determine upper bounds for the planets’ masses in the form of credible intervals on their marginal posterior distribution. As shown in Fig. 3, we derived a 90% credible interval for the planet masses of $0.20M_J \leq m_b \leq 0.23M_J$ and $0.56M_J \leq m_c \leq 0.66M_J$.

We also considered an n -body model of resonance in which opposing convergent migration and eccentricity damping forces cause planets to capture into resonance, eventually reaching equilibrium values for their semi-major axis ratio (at resonance) and their eccentricities. We proposed a simple model which treats convergent migration and eccentricity damping as exponential decay of the semi-major axis ratio and eccentricities, on timescales τ_a and τ_e respectively. By then simulating the resonance capture process using different ratios of the timescale $K = \frac{\tau_a}{\tau_e}$, different values of the planets’ eccentricities at equilibrium are obtained. We compared the resulting eccentricity track to the marginal posterior distribution of the observed eccentricities to determine if our model can explain the present orbital configuration of the system. The results of Fig. 4 suggest that the

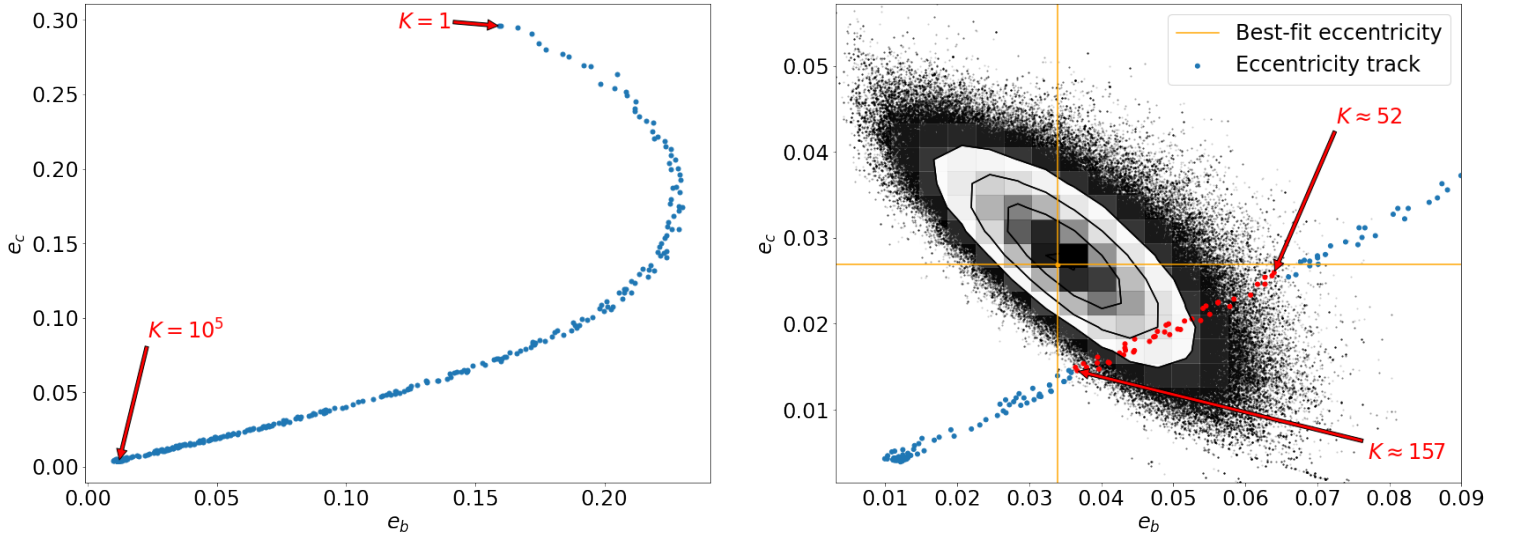


Figure 4. Comparison of our resonance capture model results with marginal eccentricity posterior. Left: Track of equilibrium eccentricities in the e_b - e_c plane, with each point on the track corresponding to the eccentricities for a different value of K . Points corresponding to $K = 1$ and $K = 10^5$ at the ends of the track are labelled, with K gradually increasing as one moves along the track from top to bottom. Right: Eccentricity track overlaid on the marginal eccentricity posterior obtained from MCMC sampling, with the best-fit eccentricity marked as well. Note that the track has been zoomed in compared to the left figure. The segment of the track marked in red are those points falling within the eccentricity posterior distribution, corresponding to values for K for which our model’s predicted equilibrium eccentricities are consistent with the currently observed eccentricities. The K values of the approximate endpoints of the overlapping track segment are labelled as well.

results of our resonance capture model match the system’s current configuration, for K in the approximate range $50 < K < 200$.

In the future, we hope that the methods used in this paper can be applied to other candidate systems with large planets in mean motion resonances (e.g. Luque et

al. (2019), Rosenthal et al. (2019), Trifonov et al. (2019), Wittenmyer et al. (2016)), in order to better understand how migration and eccentricity damping forces may affect planetary formation in general.

Software: REBOUND (Rein & Liu 2012), REBOUNDx (Tamayo et al. 2020), emcee (Foreman-Mackey et al. 2013)

REFERENCES

- Correia, A. C. M., Udry, S., Mayor, M., et al. 2009, *A&A*, 496, 521-526
- Foreman-Mackey, D., Hogg, D. W., Lang, D., & Goodman, J. 2013, *PASP*, 125, 306-312
- Goldreich, P. 1965, *MNRAS*, 130(3), 159-181
- Goldreich, P. & Tremaine, S. 1980, *ApJ*, 241, 425-441
- Hadden, S., & Payne, M. 2020, *AJ*, 160, 106
- Luque, R., Trifonov, T., Reffert, S., et al. 2019, *A&A*, 631, A136
- Perryman, M. 2018. *The Exoplanet Handbook*, 2nd ed. (Cambridge: Cambridge University Press)
- Rein, H., & Liu, S. F. 2012, *A&A*, 537, A128
- Rein, H., Papaloizou, J. C. B., & Kley, W. 2009, *A&A*, 510, A4
- Rosenthal, M. M., Jacobson-Galan, W., Nelson, B., et al. 2019, *AJ*, 158, 136
- Tamayo, D., Rein, H., Shi, P., Hernandez, D.M. 2020, *MNRAS*, 491(2), 2885-2901
- Trifonov, T., Stock, S., Henning, T., et al. 2019, *ApJ*, 157, 93
- Trifonov, T., Tal-Or, L., Zechmeister, M., et al. 2020, *A&A*, 636, A74
- Wittenmyer, R. A., Johnson, J. A., Butler, R. P., et al. 2016, *ApJ*, 818, 35

APPENDIX

A. COMPUTING INDIVIDUAL MIGRATION TIMESCALES FROM CONVERGENT TIMESCALE

In this appendix we derive the matrix equation for computing the individual migration timescales τ_{a_i} from the overall convergent migration timescale τ_a . Note that individual and convergent migration timescales all obey exponential decay of the form $a(t) = a_0 e^{-t/\tau_a}$. We first normalize the semi-major axis $a_0 = 1$, allowing us to write $\ln(a) = -\frac{t}{\tau_a}$, or:

$$\frac{d}{dt} \ln(a) = -\frac{1}{\tau_a} \quad (\text{A1})$$

We take a in the exponential decay for τ_a to be $a = \frac{a_1}{a_2}$ (the ratio of the planets' semi-major axes), meaning we can write A1 as $-\frac{1}{\tau_a} = \frac{d}{dt} \ln\left(\frac{a_1}{a_2}\right)$. This yields:

$$\begin{aligned} -\frac{1}{\tau_a} &= \frac{d}{dt} \ln\left(\frac{a_1}{a_2}\right) = \frac{\dot{a}_1}{a_1} - \frac{\dot{a}_2}{a_2} \\ &= -\frac{a_1}{\tau_{a_1} a_1} + \frac{a_2}{\tau_{a_2} a_2} \\ -\frac{1}{\tau_a} &= \frac{1}{\tau_{a_2}} - \frac{1}{\tau_{a_1}} \end{aligned} \quad \text{since } \dot{a}_i = -\frac{1}{\tau_{a_i}} e^{-t/\tau_{a_i}} = -\frac{a_i}{\tau_{a_i}} \quad (\text{A2})$$

for the individual migration timescales. We then obtain a second expression for τ_{a_i} , using conservation of total energy ($\frac{dE}{dt} = 0$):

$$\begin{aligned} E &= -\frac{1}{2} \frac{GMm_1}{a_1} - \frac{1}{2} \frac{GMm_2}{a_2} & \text{Planets have masses } m_1, m_2 \\ 0 &= \frac{1}{2} \frac{GMm_1 \dot{a}_1}{a_1^2} + \frac{1}{2} \frac{GMm_2 \dot{a}_2}{a_2^2} & \frac{dE}{dt} = 0 \\ 0 &= -\frac{m_1 a_1}{\tau_{a_1} a_1^2} - \frac{m_2 a_2}{\tau_{a_2} a_2^2} & \text{again using } \dot{a}_i = -\frac{a_i}{\tau_{a_i}} \\ 0 &= \frac{m_1}{\tau_{a_1}} + \frac{m_2}{\tau_{a_2}} \left(\frac{a_1}{a_2}\right) \end{aligned} \quad (\text{A3})$$

We then solve the system of equations A2 and A3 for $1/\tau_{a_1}$ and $1/\tau_{a_2}$:

$$\begin{aligned} \begin{bmatrix} -1 & 1 \\ m_1 & m_2 \left(\frac{a_1}{a_2}\right) \end{bmatrix} \begin{bmatrix} 1/\tau_{a_1} \\ 1/\tau_{a_2} \end{bmatrix} &= \begin{bmatrix} -1/\tau_a \\ 0 \end{bmatrix} \\ \begin{bmatrix} 1/\tau_{a_1} \\ 1/\tau_{a_2} \end{bmatrix} &= A^{-1} \begin{bmatrix} -1/\tau_a \\ 0 \end{bmatrix} \end{aligned} \quad \text{where } A = \begin{bmatrix} -1 & 1 \\ m_1 & m_2 \left(\frac{a_1}{a_2}\right) \end{bmatrix} \quad (\text{A4})$$

and we thus compute the individual migration timescales $1/\tau_{a_1}$, $1/\tau_{a_2}$ from τ_a using equation A4. We take a_1/a_2 as the resonant semi-major axis ratio of the inner to outer planet, given by $a_1/a_2 = (P_1/P_2)^{2/3}$ using Kepler's third law.